Journal Pre-proofs

Numerical analysis of compliance and fatigue life of the CCC specimen

D.M. Neto, F.V. Antunes, E.R. Sérgio, R. Branco, A. Camacho-Reyes, F. Diaz, G.L. Gómez Gonzales, J. Vasco-Olmo

PII: S0142-1123(22)00746-0
DOI: https://doi.org/10.1016/j.ijfatigue.2022.107496
Reference: JIJF 107496

To appear in: *International Journal of Fatigue*

Received Date: 15 October 2022
Revised Date: 20 December 2022
Accepted Date: 27 December 2022

Please cite this article as: Neto, D.M., Antunes, F.V., Sérgio, E.R., Branco, R., Camacho-Reyes, A., Diaz, F., Gómez Gonzales, G.L., Vasco-Olmo, J., Numerical analysis of compliance and fatigue life of the CCC specimen, *International Journal of Fatigue* (2022), doi: https://doi.org/10.1016/j.ijfatigue.2022.107496

This is a PDF file of an article that has undergone enhancements after acceptance, such as the addition of a cover page and metadata, and formatting for readability, but it is not yet the definitive version of record. This version will undergo additional copyediting, typesetting and review before it is published in its final form, but we are providing this version to give early visibility of the article. Please note that, during the production process, errors may be discovered which could affect the content, and all legal disclaimers that apply to the journal pertain.

© 2022 The Author(s). Published by Elsevier Ltd.

Numerical analysis of compliance and fatigue life of the CCC specimen

D.M. Neto[a], F.V. Antunes[a]*, E.R. Sérgio[a], R. Branco[a], A. Camacho-Reyes[b], F. Diaz[b], G.L. Gómez Gonzales, J. Vasco-Olmo[b]

[a] CEMMPRE, Centre for Mechanical Engineering, Materials and Processes, University of Coimbra, Mechanical Engineering Department, Pinhal de Marrocos, 3030-788, Coimbra, Portugal

[b] Departamento de Ingeniería Mecánica y Minera, University of Jaén, Jaén, Spain

Highlights

- The CCC specimen is a cylindrical specimen with central crack, produced by additive manufacturing.
- The compliance increases non-linearly with crack radius; the variation is small for the shorter cracks.
- An expression was proposed for the compliance, useful for the future experimental measurement of crack length.
- Fatigue life is predicted numerically using an approach based on cumulative plastic strain.

Abstract (100)

This study presents the numerical evaluation of the compliance in the CCC specimen aiming to assess the crack length inside the specimen. The numerical model considered the elastoplastic behaviour of the specimen, which is modelled using axisymmetric finite elements. The results shown that the propagation of the crack yields a non-linear increase of the compliance. Nevertheless, variation of the compliance is very small for small values of crack radius. Considering a loading sequence composed by four load blocks of constant amplitude, the fatigue crack growth was predicted both using the Paris law and the numerical model. Both

Journal Pre-proofs

predictions agree but only the numerical simulation is able to capture the crack retardation between load blocks.

Keywords: Fatigue crack growth, CCC specimen (cylindrical with central crack), compliance, numerical analysis

* Corresponding author: fernando.ventura@dem.uc.pt

Journal Pre-proofs

1. Introduction

Fatigue crack growth (FCG) is usually studied using through-thickness specimens, namely the compact tension (CT) and the middle-tension (MT) geometries. These geometries are normalised in international standards [1,2], which define not only the geometry but all testing procedure. However, the crack fronts have interior points, a near surface region and corner points. Plane strain state is supposed to occur inside the specimen, while plane stress state is expected near the surface.

Stress state has a great influence on FCG, and the first evidence of this is the tunnelling effect observed in through-thickness cracks. The effect of stress state is usually associated with crack closure phenomenon. In fact, there is a general consensus about the higher relevance of crack closure under plane stress conditions [3,4]. Besides, stress state may have a direct influence on the FCG mechanisms, as was observed in nickel base superalloys [5, 6]. In fact, the stress triaxiality observed at interior crack front positions favour diffusion-based mechanisms and void formation, while the plane stress state favours plastic deformation.

However, the coexistence of stress states imposes a complexity which is far from being understood. The relative importance of interior and surface regions on FCG is not known, and the corner points are a source of complexity. Besides, there is complex influence of loading and crack length on the extension of surface regions, and supposedly on the relative importance of plane stress and plane strain states. The application of an overload, for example, increases the surface region, as is quite evident in Figure 5 of Salvatti *et al.* [7]. The increase of crack length in also known to promote plane stress state. The thickness of the specimens is usually used to obtain dominance of one of the stress states. Specimens with a thickness of 10 mm or higher are usually assumed to have a dominance of plane strain state [8,9], while a thickness lower than 4 mm is used to obtain plane stress states [10,11]. However, the transition thicknesses are expected to be material dependent. Branco *et al.* [12] proposed a plane strain

Journal Pre-proofs

specimen geometry using lateral notches. Nevertheless, the corner points and surface regions are always present, affecting FCG in a complex and unknown way.

In a previous work [13] the authors proposed a novel specimen having pure plane strain state along the whole crack front. It is a cylindrical specimen with central crack, called CCC specimen, produced by additive manufacturing. In fact, the ability of this technology to produce parts with any shape opened up a very interesting opportunity to isolate the effect of stress state by placing a defect exactly at the centre of a cylindrical specimen. Internal cracks are also typically observed in very high cycle fatigue regime, but the initiation position is random [14,15]. This specimen opens the opportunity to study different issues of FCG under pure plane strain conditions, namely the effect of stress ratio and overloads. In the CCC specimen the crack propagates in a circular shape and supposedly in vacuum. This is interesting because avoids the use of complex and expensive vacuum chambers. The inclusion of longitudinal channels permits the access of the external environment to the internal crack, so the CCC specimens may also be used for tests in air on in controlled environment. Studies in vacuum are fundamental to understand the effect of environment on FCG. Besides, components may work in vacuum, namely in aerospace industry. The use of these specimens may be very interesting for laboratories without vacuum chambers. Anyway, the existence of vacuum in the CCC specimens without longitudinal channel must be checked by comparing the FCG results with similar ones obtained in a vacuum chamber.

The main problem in the use of this geometry is the measurement of crack length inside the specimen. In the classical geometries, crack length is usually measured using an optical microscope, however alternative approaches, namely compliance and potential drop, are widely used. For tests at elevated temperature inside a furnace, where the direct measurement of crack length is impossible, the potential drop has been used [16]. Tesch *et al.* [17] used DC potential drop method (DCPD) for an automated crack length measurement. This greatly

Journal Pre-proofs

facilitated constant K-max tests, which require an adjustment of loads with crack growth. Compliance technique is widely used in the laboratory measurement of instantaneous crack length of specimens during fatigue properties testing [18]. The specimen compliance, *C*, is defined as the slope of the linear response in terms of crack mouth opening displacement versus load records. There is a direct link between compliance and crack length, which also depends on thickness of the specimen and elastic properties of the material. The compliance of CT specimens is given in ASTM standard [1].

The main objective here is to study the measurement of crack length inside the CCC specimen using compliance measurements. An axisymmetric numerical model is used to predict specimen's rigidity and fatigue life. The numerical simulation of FCG is based on cumulative plastic strain at the crack tip. This study is carried out after the proof of concept [13], being fundamental for the use of this specimen geometry to analyse different issues of FCG. In the future, the CCC specimen is expected to play a significant role in the understanding of the effects of stress state and environment on FCG. It will be interesting to study the effects of ΔK, stress ratio, overloads and load blocks under pure plane strain state.

2. Numerical model

The numerical analysis of the fatigue crack growth in the CCC specimen was carried out using the in-house finite element code DD3IMP [19]. The numerical model takes into account the elastoplastic behaviour of the specimen while the loading (axial force) is applied under quasi-static conditions. The geometry and main dimensions of the CCC specimen are presented in Figure 1. An initial defect with a diameter of 1.5 mm was placed at the central section of the CCC specimen produced by additive manufacturing. The crack initiates from this defect and propagates in a circular shape [13]. The initial defect may have other size, but its presence is fundamental in this context. Since there is no access of the air, the crack propagates in vacuum. Similar specimens were produced with a longitudinal channel, to permit the access of the air.

The symmetry of the specimen allows to use of axisymmetric finite elements in the numerical simulation. Besides, only half-length of the specimen was modelled due to symmetry conditions, reducing the computational cost. Note that the shape of the initial notch is not being modelled in the numerical study and the cracks are assumed to be sharp. Figure 2 presents the finite element mesh of the specimen, which is composed by four-node quadrilateral axisymmetric elements. Different element sizes were adopted in order to reduce the computational time. Thus, a very refined zone with an element size of 8 μm was generated around the crack path (symmetry plane), allowing an accurate prediction of the stress and strain field at the crack tip. Away from the crack path, the element size increases gradually, as shown in Figure 2, resulting in a mesh composed by 21427 finite elements. The central crack is defined by applying adequate boundary conditions, namely the elimination of the symmetry conditions in the axial direction for the nodes covered by the crack length. The crack radius, a, which is half of the total crack length, is the distance from the center of the specimen to the crack tip.

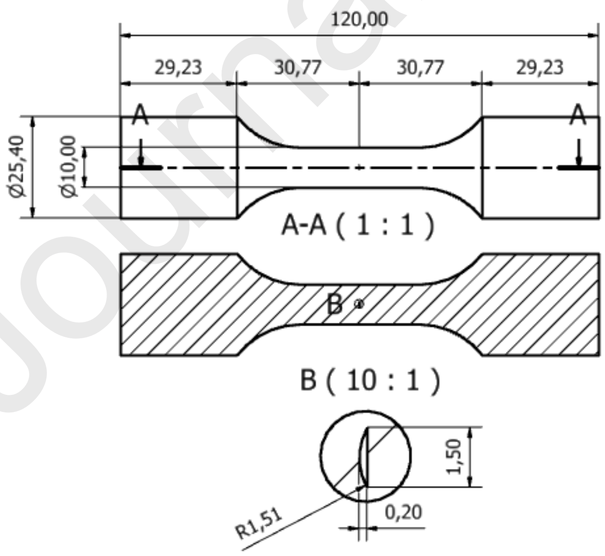

Figure 1. Geometry and main dimensions of the CCC specimen.

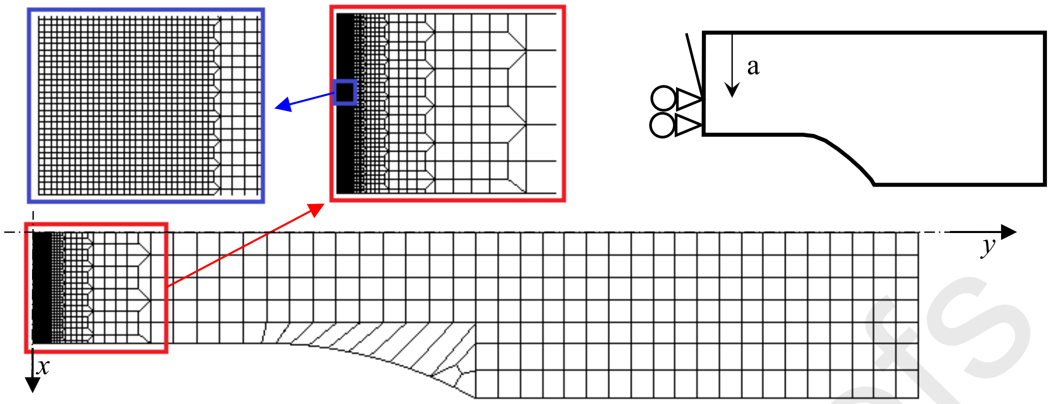

Figure 2. Finite element mesh of the CCC specimen using four-node quadrilateral axisymmetric elements.

The manufacturing of this specimen geometry requires the adoption of additive manufacturing processes, namely the selective laser melting [13]. Hence, the material studied is the aluminium alloy AlSi10Mg, which has been widely used in additive manufacturing. The elastic behaviour was modelled with the Hooke's law, considering the parameters listed in Table 1. The shape of the yield surface was defined by von Mises yield criterion, while the material work hardening was described by the Swift law [20] coupled with the Lemaitre-Chaboche law [21]. The flow stress defined by the isotropic hardening law (Swift) is given by:

$$\sigma_y = k\left(\left(\frac{Y_0}{k}\right)^{\frac{1}{n}} + \bar{\varepsilon}^{\mathrm{p}}\right)^{n} \quad (1)$$

where $\bar{\varepsilon}^p$ denotes the equivalent plastic strain and Y_0, k, and n are the material parameters of the Swift law. The evolution of the back-stress tensor defined by the kinematic hardening law (Lemaitre-Chaboche) is given by

$$\dot{\boldsymbol{X}} = C_{\mathrm{X}}\left[\frac{X_{\mathrm{sat}}}{\bar{\sigma}}(\boldsymbol{\sigma}' - \boldsymbol{X})\right]\dot{\bar{\varepsilon}}^p \quad \text{with} \quad \dot{\boldsymbol{X}}(0) = 0, \quad (2)$$

where, $\boldsymbol{X}$ is the back-stress tensor, $\boldsymbol{\sigma}'$ is the deviatoric Cauchy stress tensor, $\bar{\sigma}$ is the von Mises equivalent stress and X_{Sat} and C_{x} are material parameters. The material parameters, involved in the work hardening laws, were obtained fitting numerical stress–strain results to experimental curves obtained both in monotonic tension and low-cycle fatigue tests. The comparison between the fitted curves and experimental data is presented in Figure 3a and Figure 3b, for the monotonic tension and low-cycle cases, respectively. Since the von Mises yield criterion presents tension-compression symmetry, the low-cycle data cannot fit perfectly. Additionally, note that only the last cycle of the test was employed. The analysis of several load cycles showed a fast stabilization of material behaviour and a good agreement between experimental results and numerical predictions. The obtained set of material parameters is presented in Table 1.

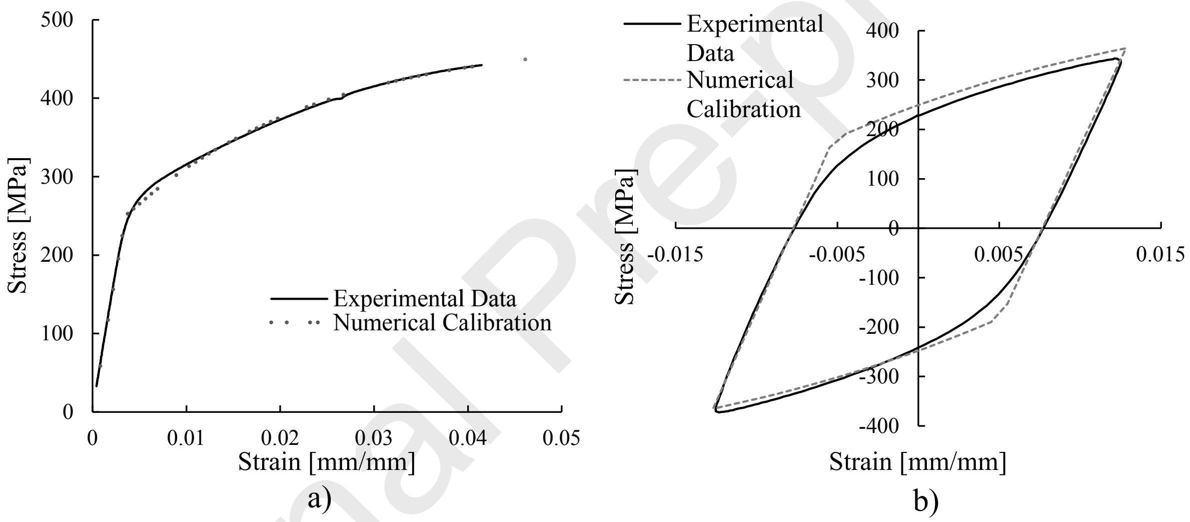

Figure 3. Comparison between the fitted curves and experimental data for: a) monotonic test; b) Low-cycle fatigue test where only the last cycle of the finite stress–strain loops is considered.

Table 1. Elastic properties of the aluminium alloy AlSi10Mg and the parameters of the work hardening laws (Swift in the isotropic hardening a Lemaitre-Chaboche in the kinematic hardening).

	E (GPa)	v (-)	Y_0 (MPa)	k (MPa)	n (-)	X_{sat} (MPa)	C_X (-)
AlSi10Mg	72	0.29	250	289.34	0.092	220.18	57.53

The crack propagation was carried out by node release along the radial direction in the symmetry plane. The crack increment is defined by the mesh size, which corresponds to 8 μm in the present model. The node release occurs at minimum load when the cumulative plastic strain at the crack tip reaches a critical value. Using a predefined value of the stress intensity factor range, approximately mid-range, the comparison between the predicted FCG rate and the experimental value allows the fitting of the critical value of plastic strain, $\varepsilon_{\mathrm{c}}^{\mathrm{p}}$. In this case both the initial guesses ($\varepsilon_{\mathrm{c}}^{\mathrm{p}} = 60\%$ and $\varepsilon_{\mathrm{c}}^{\mathrm{p}} = 200\%$) shown to provide fatigue crack growth rates below the experimental data. These values were proposed considering the critical cumulative plastic strains obtained in previous works of the authors for other materials [22,23]. This way, the critical plastic strain was identified through the intersection of the curve defined by the two initial guesses with the experimental crack growth rate defined by the horizontal line, as shown in Figure 4a). The described process provided a critical plastic strain of 35%. The numerical *da/dN*-Δ*K* curve, obtained with the calibrated $\varepsilon_{\mathrm{c}}^{\mathrm{p}}$ is compared with the experimental data for R=0.05, in Figure 4b). The numerical analysis of the crack growth was simplified by considering different initial crack sizes, a_0. The crack sizes considered were a_0=3.5, 5.5, 11.5 e 16.5 mm. This allows to evaluate relatively wide ranges of Δ*K* with the same loading case and to save computational time. As expected, both curves intersect at the ΔK value employed in the calibration process. However, above this value *da/dN* is underestimated while for smaller ΔK levels the fatigue crack growth rate is overestimated. Using the experimental data, the exponent *m* of the Paris law is 3.53, while the numerical solution leads to *m*=2.19. This difference between numerical and experimental exponents was observed in previous studies for other materials [22]. All the *da/dN* results presented in Figure 4 were obtained using CT specimens with a width W= 36 mm.

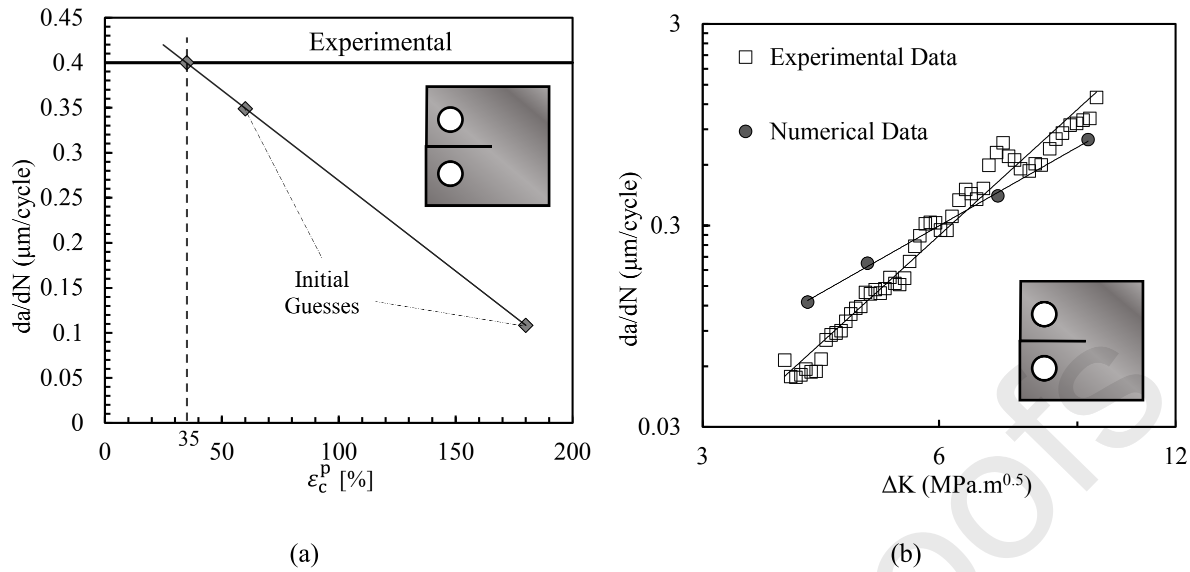

Figure 4.a) Initial guesses and calibration procedure for the critical plastic strain for this aluminium alloy ($\Delta K \cong 7$ MPa.m$^{0.5}$); **b)** Comparison between the numerical and experimental *da/dN*-Δ*K* curves for *R=0.05*.

3. Specimen compliance

Since the crack is completely inside the specimen, indirect methods are required to assess the evolution of the crack size. The stiffness of the specimen, K_s, decreases with crack length, therefore the compliance, which is the inverse of stiffness, increases as the crack length increases. The compliance of the CCC specimen was studied in detail using the numerical model previously presented. The compliance of the specimen loaded axially can be defined by:

$$C = \frac{1}{K_s} = \frac{\Delta L}{\Delta F} \tag{3}$$

where ΔL denotes the variation of specimen length produced by an increment of applied load ΔF. The stiffness of the specimen was evaluated for different values of crack radius using the minimum and maximum loads together with the change of specimen length evaluated at minimum and maximum loads. Figures 5 present the relationships between applied force and variation of specimen length obtained for different values of crack radius (a) and two load ranges. A perfect linear relation is always observed between ΔL and force, and the slope of the straight lines is the stiffness of the specimen. Increasing the applied load range from 4 kN to 8 kN, Figures 5 (a) and (b), respectively, leads to a larger change of specimen length (ΔL).

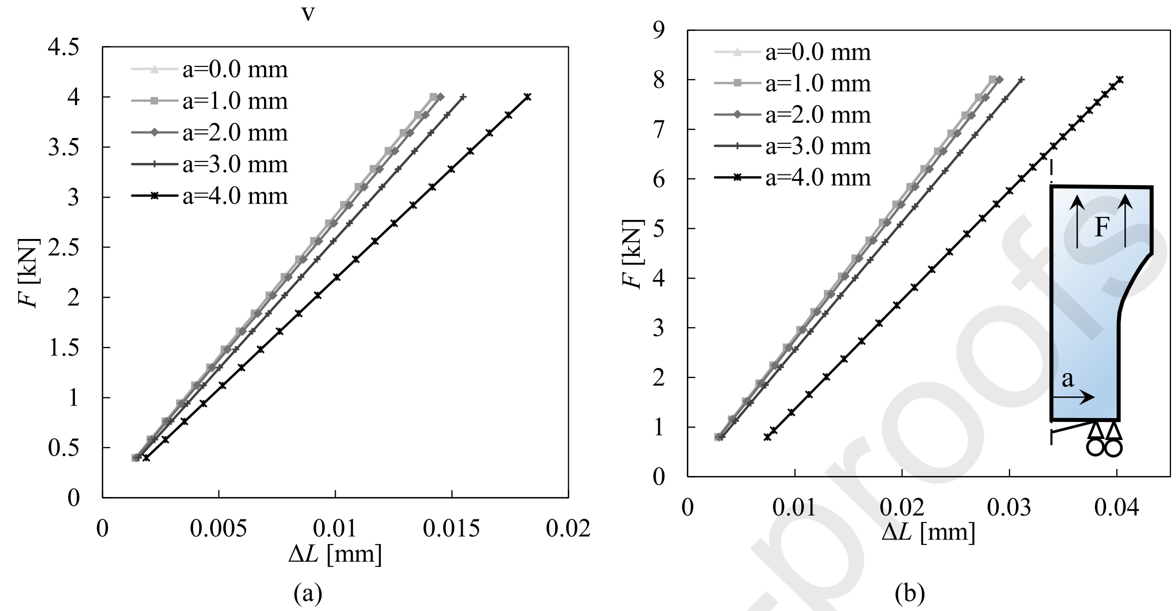

Figure 5. Relationship between applied force and variation of specimen length (L_0 = 20 mm) evaluated numerically after 5 load cycles for R=0.1 using different loading ranges: (a) F_{max} = 4 kN; (b) F_{max} = 8 kN.

The compliance value depends not only on crack length, but also on the initial length L_0 used to measure ΔL on the material's rigidity and on specimen's geometry. In fact, ΔL is proportional to L_0 under a linear elastic regime for a constant cross-section of the specimen. Therefore, as is evident in Equation 3, the increase of L_0 increases the compliance. Considering the dimensions of the CCC specimen (Figure 1), namely the gauge length, the compliance was evaluated for L_0=20 mm, which is the initial gauge length of the clip-gauge extensometer available for the future experimental work. On the other hand, the compliance value of the specimen is independent of the load applied under the linear elastic regime. In fact, in Figures 5, for each crack length the slope of the straight lines does not change with load level.

The most relevant parameter influencing compliance is, however, the crack length. Figures 6 (a) and (b) present the stiffness and the compliance, respectively, evaluated from the numerical predictions presented in Figures 5. The propagation of the crack yields a reduction of the stiffness and a consequent increase of the compliance. The variations are very weak for the short crack radii, increasing progressively with crack radius. The effect of the load range on both stiffness and compliance is negligible. This aspect is relevant since the plastic zone deformation arising near the crack tip could change the stiffness of the CCC specimen. This issue was studied considering two load ranges and calculating the compliance only after 5 load cycles, aiming the stabilization of the plastic zone. As can be seen in Figures 5, despite the localized plastic deformation around the crack tip, a linear relationship was always observed between the applied load and the variation of specimen length. The plastic deformation around the crack tip leads to a horizontal translation of the curve to the right side, i.e. the initial length is not recovered when the load is removed due to the localized plastic deformation. This is particularly evident for large values of crack radius and large values of load (Figure 5 (b)). However, the coincidence of results for the two load ranges observed in Figure 6 indicates that the crack tip plastic deformation is not affecting specimen's compliance. Hence, this parameter is mainly dictated by the elastic properties of the aluminium alloy (see Table 1) and specimen geometry. The fitting of the results obtained by numerical simulation allows to define an equation for the compliance of the CCC specimen, which is given by:

$$C = \frac{L_0}{E}\left(20.76\lambda^3 - 18.16\lambda^2 + 6.66\lambda + 11.98\right)\ [\mathrm{mm/kN}] \tag{4}$$

where E denotes the Young modulus [MPa], L_0 is the initial length [mm] and $\lambda = a/R$. The polynomial fitting was obtained for $0.2<\lambda<0.8$.

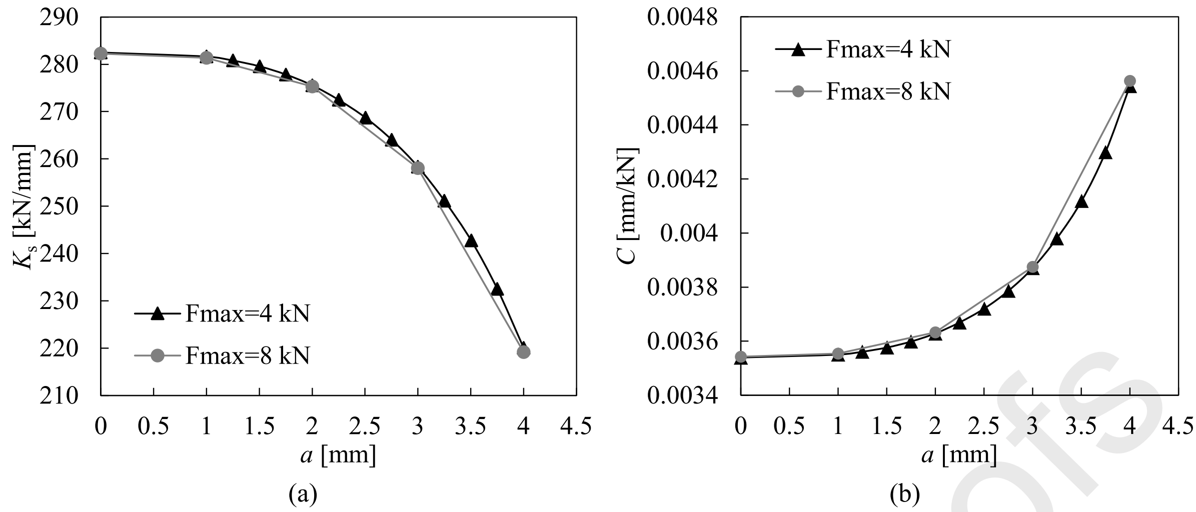

Figure 6. Influence of the crack length on both stiffness and compliance, evaluated numerically in a portion of the specimen with L_0 = 20 mm for two different values of loading range using R=0.1: (a) stiffness; (b) compliance.

Since the variation of the compliance is very small for small values of crack size (see Figure 6 (b)), the sensibility of the measurement technique is an important issue. In fact, for *a*=2 mm the compliance increased only 2.5% in comparison with the situation without crack (*a*=0). On the other hand, for *a*=3.5 mm the compliance increased more than 16% in comparison with the situation without crack. Therefore, the use of the compliance to assess the crack size in CCC specimens requires the adoption of experimental techniques with high sensibility, particularly for small values of crack size.

Equation 4 is fundamental for the determination of crack length from experimental values of compliance. However, assuming deterministic values of load and considering an absolute uncertainty of ±0.3 μm in the measurement of ΔL, the experimental compliance contains an uncertainty. This is the uncertainly expected for the clip-gauge extensometer which will be used in the future experimental work. Figure 7 (a) presents the evolution of ΔL predicted during the crack propagation, obtained for the two different loading range values. Thus, the well-defined relationship between the compliance and the crack size (Figure 6 (b)) becomes unclear. In other words, the evaluation of crack radius from compliance is affected by the uncertainty in the measurement of ΔL, and the results in Figure 7 (a) can be used to obtain a range for the inferred crack radius.

The uncertainty of ΔL was used to modify the results of Figure 6 (b) in order to have an uncertainly in the range of the values of compliance. From this plot, the uncertainty of crack length was calculated for each value of compliance. Figure 7 (b) presents the range of the inferred crack radius, for the two different loading range values. The Δa evolution was calculated using a cubic polynomial fitting applied to discrete values obtained in the numerical simulation. Since the polynomial approximation presents an inflection point near the horizontal region of the curve, the accuracy of the obtained Δa values was negatively affected by the interpolation method for a <2 mm. This is the reason for the parabolic evolution up to a=2 mm, where the inclusion of the dashed lines intends to give the probable trend of Δa for small values of crack radius. The impact of the uncertainty in the measurement is smaller for large values of applied load range. Indeed, doubling the applied load leads to a reduction of Δa to half. Besides, increasing the crack radius leads to a reduction of the uncertainty due to the increase of the of ΔL values. Therefore, the loading spectrum adopted in the fatigue crack growth must be decreasing in range to minimize the uncertainty in the measurements. For $F_{\max}$ = 8 kN, R=0.1, and a crack radius of 3 mm, the uncertainty in crack radius is 103 µm. On the other hand, for $F_{\max}$ = 4 kN, R=0.1 and a=2 mm, the uncertainty of crack radius inferred from the compliance is 727 µm.

Journal Pre-proofs

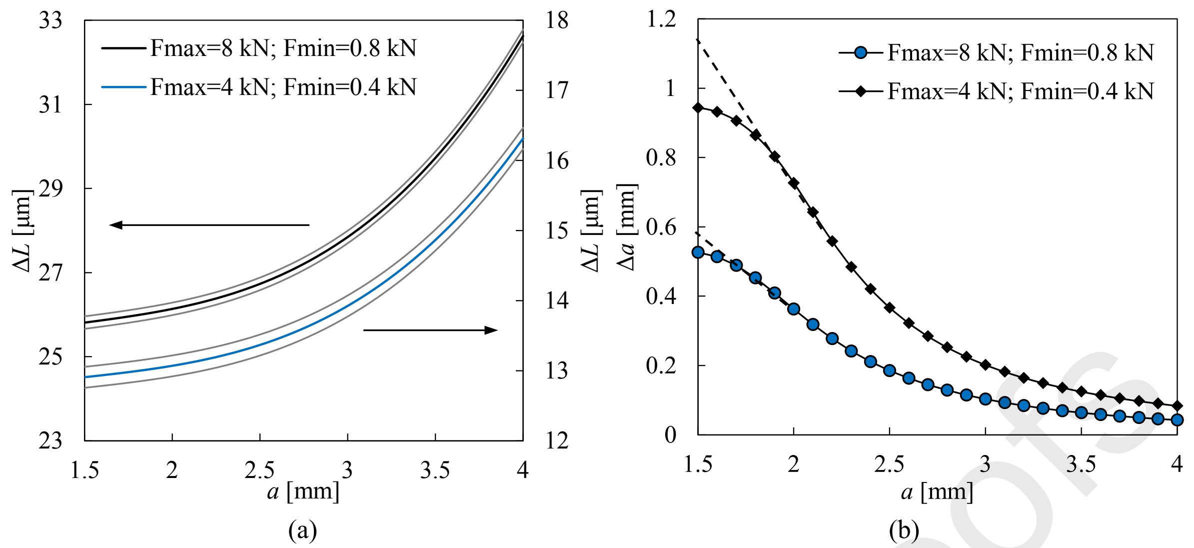

Figure 7. Influence of the load range on the uncertainty in measurement of the compliance: (a) specimen length variation with uncertainty of ±0.3 μm; (b) range of the inferred crack radius.

4. Expected fatigue life

The fatigue life of the specimen, measured in number of cycles, is composed of the crack initiation and crack propagation portions. The initiation life is commonly predicted based on the stress-life or strain-life curve obtained from smooth specimen fatigue tests. On the other hand, the propagation life is commonly predicted based on the Paris law. The fatigue life is directly dictated by the loading spectrum used in the CCC specimen. Thus, two loading spectra were analysed, which were defined by four load blocks of constant amplitude and stress ratio R=0.1. A stress ratio of 0.05 was used for calibration of the critical cumulative plastic strain. However, this is expected to be a material property, therefore can be applied to other load ratios. The first load bock is identical in both loading cases, presenting a maximum value of 11 kN. Figure 8 presents the loading spectra adopted in the study, considering both 15% and 20% of amplitude reduction between consecutive blocks. The transition between load block occurs for predefined values of crack radius.

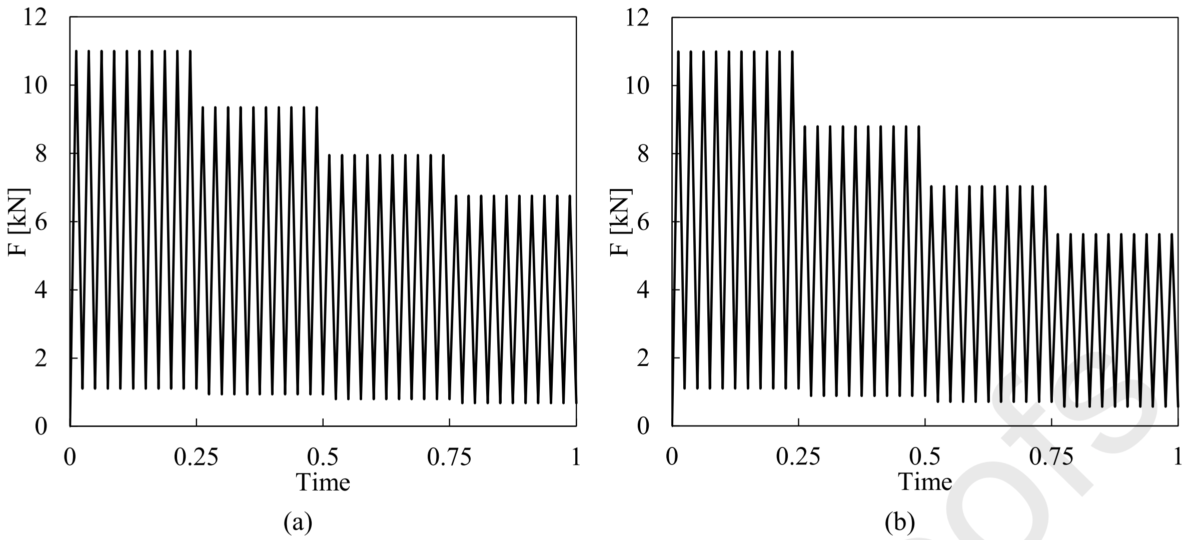

Figure 8. Definition of loading spectrum used in the CCC specimen composed by four load blocks of constant amplitude and R=0.1: (a) 15% of amplitude reduction between consecutive blocks; (b) 20% of amplitude reduction between consecutive blocks.

4.1. Fatigue initiation life

The prediction of fatigue crack initiation life was carried out using the Theory of Critical Distances (TCD). This concept gathers a group of average stress methods (e.g. Point Method, Line Method, Area Method, and Volume Method) which assume that fatigue failure takes place when a critical point, line, area or volume of the material at the notch region is subjected to a critical stress [24]. Recent studies have revisited the original idea and have introduced new approaches based on strain and energy parameters [25-26].

In this work, the analysis is carried out using the Line Method (LM) combined with the Smith-Watson-Topper (SWT) parameter, whose predictive capability has been already demonstrated in the context of additively manufactured materials [24]. The effective value of the SWT parameter (SWT_{eff}) is estimated along a straight line, emanating from the notch bisector, over a distance equal to $2a_0$:

$$SWT_{\text{eff}} = \frac{1}{2a_0}\int_0^{2a_0} SWT(r)\, dr \tag{5}$$

where SWT(r) is the distribution of the SWT parameter along the above-defined straight line, and a_0 is the so-called El-Haddad equation:

$$a_0 = \frac{1}{\pi}\left(\frac{\Delta K_{\mathrm{th}}}{\Delta\sigma_0}\right)^2 \tag{6}$$

where ΔK_{th} represents the stress intensity factor range threshold, and $\Delta\sigma_0$ is the material plain fatigue limit. These two fatigue properties must be calculated at the same stress ratio of the notched component to be assessed. For the tested material, in the as-built condition, ΔK_{th}= 0.91 MPa $m^{0.5}$ and $\Delta\sigma_0$ = 50 MPa, which corresponds to a a_0 = 1.05 mm [27-28].

The SWT parameter distribution emanating from the notch bisector, $SWT(r)$, was simulated numerically using both the mesh and elastic-plastic constitutive approach described in Section 2. Despite using the same mesh, a semi-circular notch was considered because addictive manufacturing processes are usually unable to produce sharp notches (see Figure 9). The simulations were carried out assuming a maximum force of 11 kN and R=0.1.

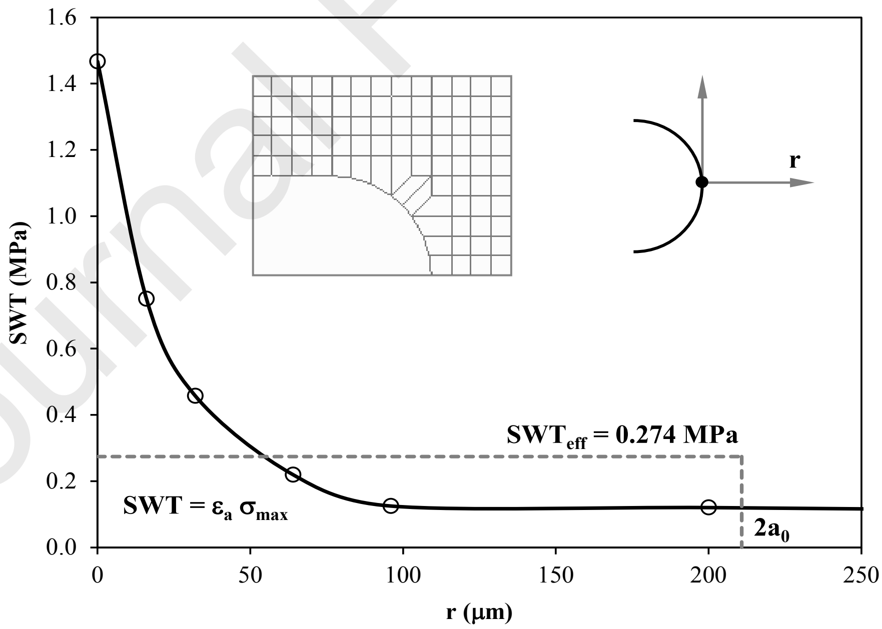

Figure 9. SWT parameter versus distance from the notch root along a straight line emanating from the notch bisector.

Figure 9 shows the distribution of the SWT parameter near the notch root along a straight line emanating from the notch bisector. In this geometry, the straight line is normal to the main axis of the specimen. As shown, the maximum value occurs at the root of the geometric discontinuity and then gradually decreases to an asymptotic value where the notch effect is no longer acting. The effective value of the SWT parameter, as represented in the figure, was equal to 0.274 MPa. In a second stage, this effective value of energy was inserted into Eq. (7) for estimating the fatigue crack initiation life (N_f):

$$SWT = \varepsilon_a \sigma_{max} = \frac{(\sigma'_f)^2}{E} (2\mathrm{N_f})^{2b} + \sigma'_f \, \varepsilon'_f \, (2\mathrm{N_f})^{b+c} \tag{7}$$

where ε_a is the strain amplitude, σ_{max} is the maximum stress, σ'_f is the fatigue strength coefficient, b is the fatigue strength exponent, ε'_f is the fatigue ductility coefficient, and c is the fatigue ductility exponent. The constants for the tested material, which are listed in Table 2, were determined from standard low-cycle fatigue tests conducted by our research group. These tests were conducted under fully-reversed strain-controlled conditions (i.e. $R_e = -1$) at a constant strain rate ($de/dt = 8\times10^{-3}\ s^{-1}$) using smooth cylindrical specimens. More details about the determination of such constants can be found in Fernandes *et al.* [29]. Solving Eq. (7), N_f is equal to 38,804 cycles.

Table 2. Fatigue strength and fatigue ductility constants [29].

σ'_f (MPa)	b	ε'_f	c
861.58	-0.168	3.78	-0.853

4.2. Fatigue propagation life using ΔK

The FCG rate can be predicted by integrating the Paris law, allowing an estimation for the crack propagation life. However, this requires knowing the stress intensity factor of the

CCC specimen. Fortunately, it is possible to find solutions in literature for interior circular cracks in cylindrical specimens axially loaded. Benthem [30] proposed the following solution:

$$K = Y\sigma\sqrt{\pi a}\,\frac{\sqrt{1-\lambda}}{1-\lambda^2} \tag{8}$$

where the remote stress is given by:

$$\sigma = \frac{F}{\pi R^2} \tag{9}$$

and the geometric factor is defined by:

$$Y = \frac{2}{\pi}\left(1 + 0.5\lambda - \frac{5}{8}\lambda^2 + 0.268\lambda^3\right) \tag{10}$$

where F is the applied force, R is specimen's radius (see Figure 10a) and λ=a/R. Recently, Alegre *et al.* [31] calculated the K value using the path independent J-integral parameter. Hence, the stress intensity factor is obtained using:

$$K = Y\sigma\sqrt{\pi a} \tag{11}$$

The remote stress is also given by equation (4) while the geometric factor can be fitted by a polynomial function:

$$Y = 1.9619\lambda^4 - 1.7342\lambda^3 + 0.7541\lambda^2 - 0.1103\lambda + 0.6424 \tag{12}$$

whose solution was defined for $\lambda \leq 0.8$. The average difference between Alegre's solution and Benthem's solution is only 0.39%, which is a good indication for the accuracy of both solutions.

The evolution of the stress intensity factor of the CCC specimen is presented in Figure 10 (a) for an axial load F=11 kN and R=5 mm. On the other hand, Figure 10 (b) presents the comparison of the K solutions for three different specimens, namely the CT specimen, the MT specimen and the CCC specimen. The load and geometry of the specimens were adjusted in order to have the same value of K for λ=0.1. Regarding the CT specimen, the load was P= 2200 N and the geometry defined by W=36 mm and B=10 mm. Regarding the MT specimen, the load was F= 18.8 kN and the geometry defined by W=50 mm and B=10 mm. The CCC specimen presents the slowest increase of K as a function of the crack radius. Besides, the trend is similar to the one obtained with the MT specimen, which is associated with the internal position of the crack and axial loading in both cases. In contrast, the CT specimen presents a quicker increase of K due to the bending effect.

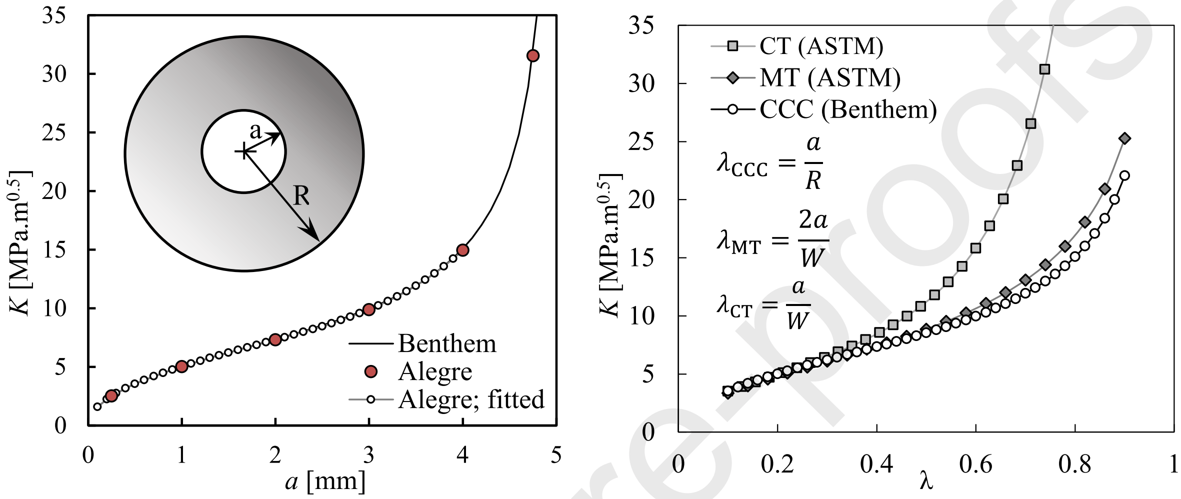

Figure 10. Analytical solutions for the stress intensity factor: (a) CCC specimen; (b) comparison of K solutions with other specimen geometries.

The increase of crack radius in the CCC specimen leads to an increase of K according to the evolution presented in Figure 10 (a). On the other hand, the decreasing block-loading sequences defined in Figure 8 allow a decrease of the K between consecutive load blocks. Therefore, the evolution of the stress intensity factor range with the crack radius is presented in Figure 11 considering that the transition between load blocks occurs for a=2.0 mm, a=2.75 mm and a=3.5 mm. These values were selected aiming for an even distribution of the marking produced by the high-low amplitude block loadings. Adopting the load sequence with 20% of amplitude reduction between consecutive blocks (Figure 8 (b)), the stress intensity factor range is larger than 5 $MPa.m^{0.5}$ and lower than 6.5 $MPa.m^{0.5}$ for the two intermediate load blocks, as shown in Figure 11 (b).

Journal Pre-proofs

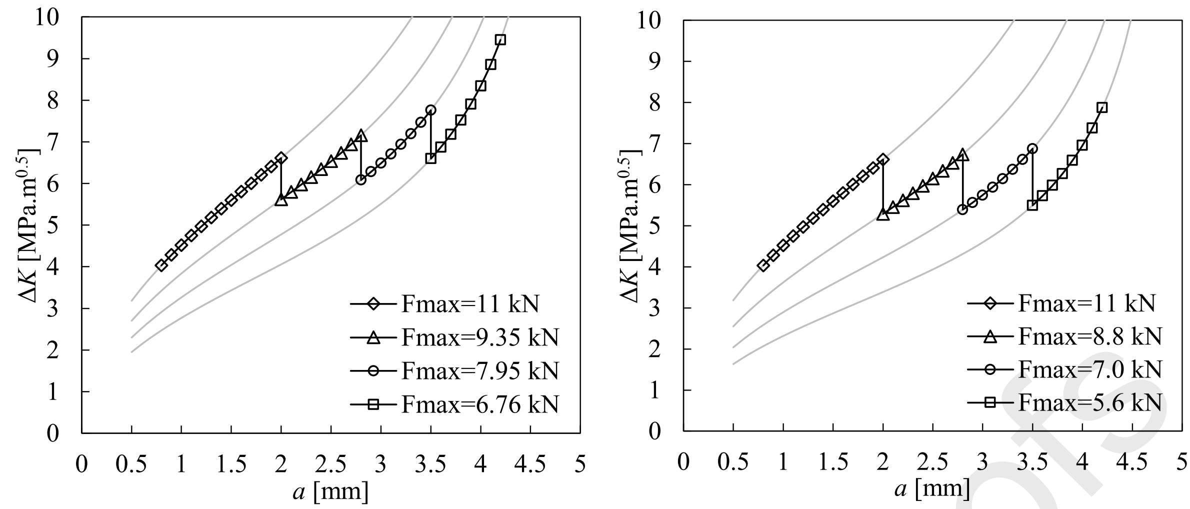

(a) (b)

Figure 11. Evolution of the stress intensity factor range with the crack radius: (a) 15% of amplitude reduction between consecutive blocks; (b) 20% of amplitude reduction between consecutive blocks.

Using the evolution of the stress intensity factor range presented in Figure 11 and assuming that the FCG is defined through the Paris law, the variation of crack radius with the number of load cycles can be estimated by the Paris law. The parameters were obtained by fitting using the experimental data da/dN-ΔK obtained in CT specimen for R=0.05 (see Figure 4 (b)). The obtained equation for the FCG rate is:

$$\frac{da}{dN} = 5\times10^{-7}(\Delta K)^{3.53} \text{ [mm/cycle]} \tag{13}$$

The variation of crack radius with the number of applied load cycles calculated from the integration of Eq. (8) is presented in Figure 12 for both load spectra analysed. Since the stress intensity factor range is globally lower when the amplitude of the load sequence decreases 20% between consecutive blocks (Figure 11 (b)), the obtained crack propagation life is higher. Starting from a crack size of *a*=0.75 mm, the total number of cycles required to achieve a crack radius of 4 mm is about 12,100 and 14,300 for 15% and 20% of amplitude reduction between consecutive blocks, respectively.

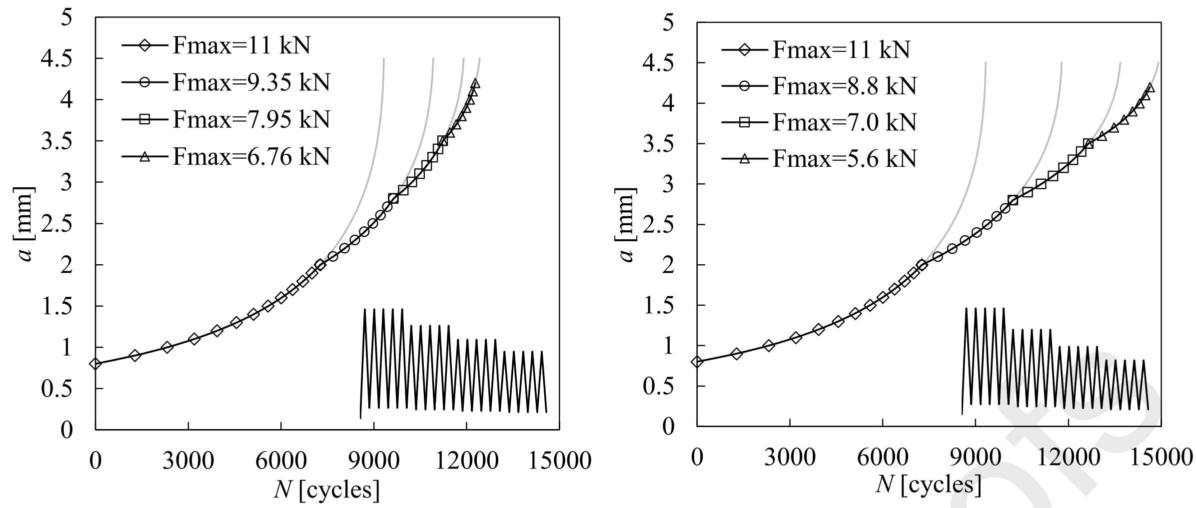

Figure 12. Variation of the crack radius with the number of load cycles: (a) 15% of amplitude reduction between consecutive blocks; (b) 20% of amplitude reduction between consecutive blocks.

Using the Paris law, the evolution of the calculated FCG rate as a function of the crack radius is presented in Figure 13, for both load spectra studied. In each load block, the increase of the crack radius leads to an increase of the FCG rate. After the first load block, the relationship between FCG rate and crack radius is approximately linear since the stress intensity factor range also rises roughly linearly within each load block (see Figure 11). In fact, the load spectrum with 20% of amplitude reduction between consecutive blocks provides a FCG rate evolution that is identical in the second and third load blocks. Thus, the selected decreasing block-loading sequence of load (see Figure 8 (b)), together with the proper crack radius transition between load blocks yields the same order of magnitude for the FCG rate evolution.

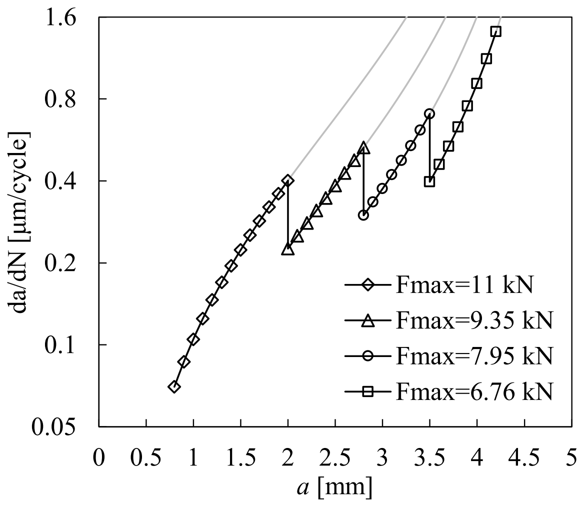

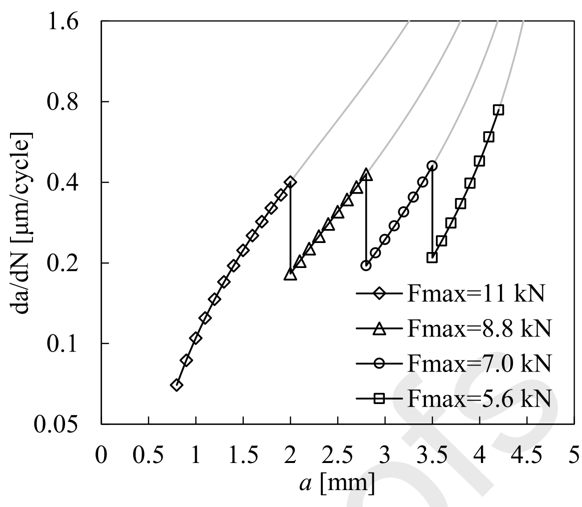

Figure 13. FCG rate as a function of the crack radius: (a) 15% of amplitude reduction between consecutive blocks; (b) 20% of amplitude reduction between consecutive blocks.

4.3. Fatigue propagation life using non-linear parameters

The direct integration of da/dN-ΔK (Paris law) carried previously does not include crack closure effects. Therefore, the numerical model was used to predict the FCG rate in the CCC specimen, as well as the effect of load blocks, namely the crack retardation in high-low amplitude block loadings. The numerical approach based on cumulative plastic strain at the crack tip is very robust, and good agreements were found between numerical predictions and experimental results obtained for load blocks [32] and overloads [33]. This clearly indicates that cyclic plastic deformation is the main damage mechanisms responsible for FCG. Using the numerical model, it was possible to conclude that there is damage below crack opening and that the effect of overloads is linked to crack closure [34].

Figure 14 presents the numerical prediction of the crack radius evolution with the number of load cycles. For both load spectra studied, the numerical predictions agree with the estimation based on the Paris law. Indeed, the maximum difference in the predicted crack radius is lower than 10%, occurring for the load spectrum with 15% of amplitude reduction between consecutive blocks. Numerical predictions are more reliable than ΔK based results as they include the effects of plasticity-induced crack closure, partial closure, crack tip blunting, and residual stresses. In fact, K-based approaches have an important limitation, which is that they do not allow the understanding of the mechanisms acting at the crack tip which are responsible for FCG.

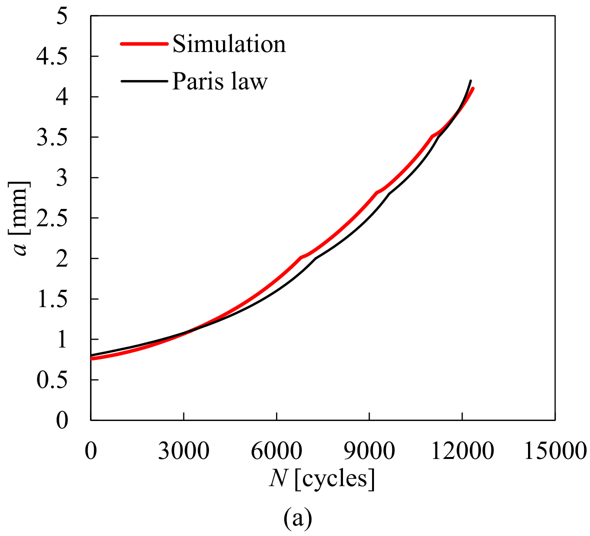

Figure 14. Numerical prediction of the crack radius evolution with the number of load cycles: (a) 15% of amplitude reduction between consecutive blocks; (b) 20% of amplitude reduction between consecutive blocks.

The numerical prediction of the FCG rate as a function of the crack radius is presented in Figure 15, which is compared with the estimation based on the Paris law. The numerical predictions agree with the Paris law estimative, particularly for the load spectrum with 20% of amplitude reduction between consecutive blocks (see Figure 15 (b)). Since the Paris law was fitted from the experimental data (Figure 4 (b)), globally the numerical model yields an overprediction of the FCG rate for small values of ΔK and an underprediction for large values of ΔK. The numerical model captured the crack retardation at the transition between load blocks, i.e. the FCG rate presents an abrupt reduction immediately at the beginning of each load block. The transient behaviour is stronger for the loading case with large amplitude variation, where the minimum FCG rate is approximately 0.06 μm/cycle (see Figure 15 (b)). Nevertheless, the extent of crack propagation affected by the transient behaviour of the high-low amplitude block loadings is relatively small. This short effect is explained by the plane strain state which is expected along all crack front of the CCC specimen.

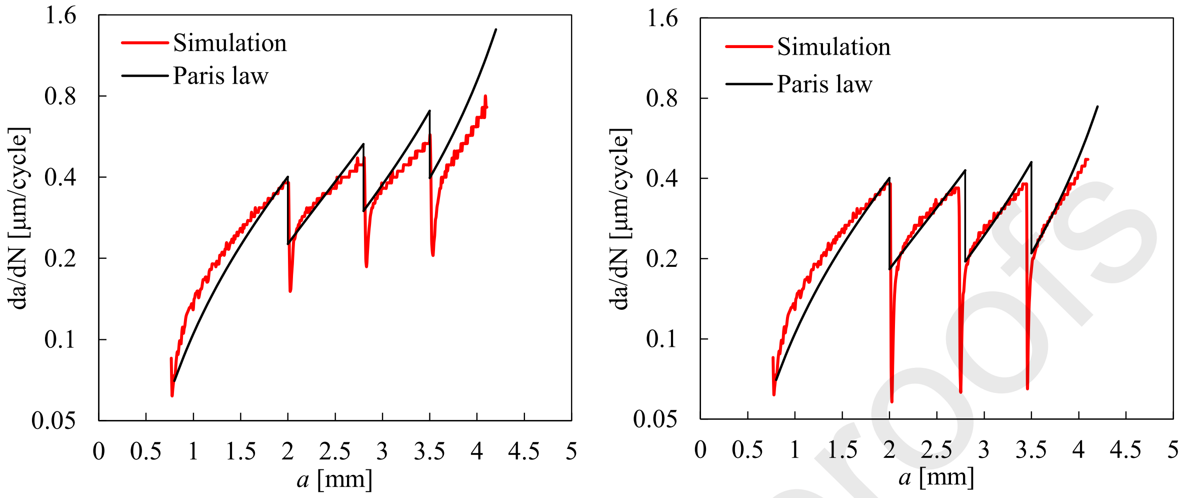

Figure 15. Numerical prediction of the FCG rate as a function of the crack radius: (a) 15% of amplitude reduction between consecutive blocks; (b) 20% of amplitude reduction between consecutive blocks.

5. Conclusions

The compliance of the CCC specimen was studied numerically for two loading ranges (F_{max} = 4 kN and F_{max} = 8 kN, R=0.1) and different values of crack radius. A measurement length L_0=20 mm and an uncertainty of ±0.3 µm in the measurement of ΔL were assumed, which are the parameters of the clip-gauge extensometer available for the future experimental work. A linear relationship between the applied load and the variation of specimen length was always obtained. Thus, compliance is independent of load range and therefore of crack tip plastic deformation. The compliance increases non-linearly with crack radius, but its variation is very small for small values of crack size. The evaluation of crack radius from compliance is affected by the uncertainty in the measurement of ΔL. The effect of this uncertainty reduces with the increase of load range and crack radius. For F_{max} = 8 kN, R=0.1, and a crack radius of 3 mm, the uncertainty in crack radius is 103 µm.

The predicted fatigue crack initiation life of the CCC specimen was 38,804 cycles for a maximum force of 11 kN and R=0.1. The fatigue crack propagation was evaluated under a decreasing loading spectrum (four load blocks of constant amplitude and R=0.1), providing a global slow increase of the stress intensity factor during the crack propagation. Then, the FCG rate evolution was predicted using the numerical model based on the cumulative plastic deformation at the crack tip, highlighting the crack retardation produced by the high-low block loadings. This transient behaviour is stronger for the load case with large amplitude variation between consecutive load blocks, but the extent of crack propagation affected is always relatively small. This short distance effect is explained by the plane strain state which is expected along all crack front of the CCC specimen.

Experimental work was planned to complement the numerical study and the CCC specimens were produced. However, the additive manufacturing process eliminated the internal defect proposed, as its thickness was too small. Thus, experimental work is directed towards future work and thicker initial defects are being considered.

Acknowledgements

The authors gratefully acknowledge the financial support through the Portuguese Foundation of Science and Technology (FCT) under the projects UIDB/00285/2020 and LA/P/0112/2020. Edmundo Sérgio is also grateful to the FCT for the PhD grant with reference 2022.11438.BD. The authors also want to acknowledge the financial support from Junta de Andalucía and through the research project "1380786" funded by Programa Operativo FEDER Andalucía 2014-2020 and from Ministerio de Universidades del Gobierno de España through the program 'Recualificación del sistema universitario Español 2021-2023: ayudas Maria Zambrano'

References

[1] ASTM E 647-11: Standard test method for measurement of fatigue crack growth rates. Philadelphia: American Society for Testing and Materials. **2011**, ASTM.

Journal Pre-proofs

[2] ISO 12108. Metallic materials – fatigue testing – fatigue crack growth method. Geneva: International Organization for Standardization (ISO). 2012.

[3] Ewalds HL, Furnée RT. Crack closure measurements along the crack front in center cracked specimens. Int. J. Fract. 1978;14:R53-R55.

[4] Matsuoka S, Tanaka K. The influence of sheet thickness on delayed retardation phenomena in fatigue crack growth in HT80 steel and A5083 aluminium alloy. Engng Fract Mech 1980;13:293-306.

[5] Antunes FV, Ramalho AL, Ferreira JAM. Identification of Fatigue Crack Propagation Modes with Roughness Measurements. Int J Fatigue 2000;22:781-788.

[6] Antunes FV, Ferreira JAM, Branco CM, Byrne J. Influence of stress state on high temperature fatigue crack growth in Inconel 718. Fatigue Fract Engng Mater Struct 2001;24:127-135.

[7] Salvati E, Zhang H, Fong KS, Song X, Korsunsky AM. Separating plasticity-induced closure and residual stress contributions to fatigue crack retardation following an overload. J Mech Phys Solids 2017; *98*:222–235.

[8] Shercliff HR, Fleck NA. Effect of specimen geometry on fatigue crack growth in plane strain – II overload response. Fatigue Fract Engng Mater Struct 1990;*13(3)*:297-310.

[9] Bichler Ch., Pippan R. Effect of single overloads in ductile metals: A reconsideration. Engng Fract Mech 2007;*74*:1344–1359.

[10] Daneshpour S, Koçak M, Langlade S. Horstmann M. Effect of overload on fatigue crack retardation of aerospace Al-alloy laser welds using crack-tip plasticity analysis. Int J Fatigue 2009;*31*:1603–1612.

[11] Zheng S, Yu Q, Gao Z, Jiang Y. Loading history effect on fatigue crack growth of extruded AZ31B mgnesium alloy. Engng Fract Mech 2013;114:42–54.

[12] Branco R, Silva JM, Infante V, Antunes FV, Ferreira F. Using a standard specimen for crack propagation under plane strain conditions. Int J Structural Integrity 2010;1(4):332-343.

[13] Jesus J, Borges MF, Antunes FV, Ferreira JAM, Reis L. A Novel Specimen Produced by Additive Manufacturing for Pure Plane Strain Fatigue Crack Growth Studies. Metals 2021;11:433. https://doi.org/10.3390/met11030433

[14] Nishijima S, Kanazawa K. Stepwise S–N curve and fish-eye failure in gigacycle fatigue. Fatigue Fract Eng Mater 1999;22:601–7.

[15] Saka, T. Review and prospects for current studies on very high cycle fatigue of metallic materials for machine structural use. J Solid Mech Mater Eng 2009;3:425–39

[16] Tong J, Byrne J. Effects of frequency on fatigue crack growth at elevated temperature. Fat Fract Engng Mater Struct 1999;22(3):185-193.

[17] Tesch A, Pippan R, Doker H. New testing procedure to determine da/dN–DK curves at different, constant R-values using one single specimen. Int J Fatigue 2007;29:1220–1228.

[18] Nakai Y, Hirai T, Kikuchi S. Compliance method to measure crack length and crack closure for automated fatigue crack propagation test of nanocrystalline nickel film. Engng Fract Mech 2021;254:107925.

[19] Menezes LF, Teodosiu C. Three-dimensional numerical simulation of the deep-drawing process using solid elements. J Mater Process Tech 2000;97:100–106.

[20] Swift HW. Plastic instability under plane stress. J Mech Phys Solids 1952;1:1–18.

[21] Frederick CO, Armstrong PJ. A mathematical representation of the multiaxial Bauschinger effect. Mater High Temp 2007;24:1–26.

Journal Pre-proofs

[22] Borges MF, Neto, DM, Antunes FV. Numerical simulation of fatigue crack growth based on accumulated plastic strain. Theor Appl Fract Mech 2020;108:102676.

[23] Antunes, F. V., S. M. Rodrigues, R. Branco, and D. Camas. A numerical analysis of CTOD in constant amplitude fatigue crack growth. Theoretical and Applied Fracture Mechanics 2016;85: 45-55.

[24] Taylor D. The theory of critical distances. Eng Fract Mech 2008;75:1696-1705.

[25] Zhu SP, Liu Y, Liu Q, Yua ZY. Strain energy gradient-based LCF life prediction of turbine discs using critical distance concept. Int J Fat 2018;113:33-42.

[26] Branco R, Costa JD, Martins Ferreira JA, Capela C, Antunes FV, Macek W. Multiaxial fatigue behaviour of maraging steel produced by selective laser melting. Mater Des 2021;201:109469.

[27] Ribeiro R. Fatigue crack propagation in aluminum specimens produced by additive manufacturing: effect of heat treatment. Department of Mechanical Engineering, University of Coimbra, MSc thesis, 2022 [in Portuguese].

[28] Pires M. Effect of different geometric discontinuities and heat treatments on fatigue strength of AlSi10Mg aluminum alloy samples produced by SLM. Department of Mechanical Engineering, University of Coimbra, MSc thesis, 2022 [in Portuguese].

[29] Fernandes RF, Jesus JS, Branco R, Borrego LP, Costa JD, Ferreira JAM. Influence of post-processing heat treatment on the cyclic deformation behaviour of AlSi10Mg aluminium alloy subjected to laser powder bed fusion. Int J Fat 2022;164:107157.

[30] Benthem JP, Koiter WT. Asymptotic approximations to crack problems. In: Sih, G.C. (eds) Methods Anal. Solut. Crack Probl. Mechanics of fracture, vol 1. Springer, Dordrecht. 1973. https://doi.org/10.1007/978-94-017-2260-5_3.

[31] Alegre JM, Cuesta II, Díaz A. Stress-intensity factor solutions for embedded elliptical cracks in round bars subjected to tensile load. Theor Appl Fract Mech 2022;117;103189.

[32] Neto DM, Sérgio ER, Borges MF, Borrego LP, Antunes FV. Effect of load blocks on fatigue crack growth. Int J Fatigue 2022;162:107001.

[33] Neto DM, Pedro J, Borges MF, Borrego LFP, Sérgio ER, Antunes FV. Numerical prediction of fatigue crack growth based on cumulative plastic strain versus experimental results for AA6082-T6. Int J Fract 2020;108:102676.

[34] Borges MF, Neto DM, Antunes FV. Revisiting Classical Issues of Fatigue Crack Growth Using a Non-Linear Approach. Materials 2020;13:5544.

Journal Pre-proofs

Declaration of interests

The authors declare that they have no known competing financial interests or personal relationships that could have appeared to influence the work reported in this paper.

Journal Pre-proofs